Journal of Statistical Mechanics:
Theory and Experiment

Short-time large deviations of the spatially averaged height of a Kardar–Parisi–Zhang interface on a ring

OPEN ACCESS

Journal of Statistical Mechanics: Theory and Experiment
An IOP and SISSA journal

PAPER: Classical statistical mechanics, equilibrium and non-equilibrium

Short-time large deviations of the spatially averaged height of a Kardar–Parisi–Zhang interface on a ring

Timo Schorlepp[1,*], **Pavel Sasorov**[2] and **Baruch Meerson**[3]

[1] Institute for Theoretical Physics I, Ruhr University Bochum, 44801 Bochum, Germany
[2] ELI Beamlines Facility, ERIC, 25241 Dolní Břežany, Czech Republic
[3] Racah Institute of Physics, Hebrew University of Jerusalem, Jerusalem 91904, Israel
E-mail: timo.schorlepp@rub.de

Received 17 July 2023
Accepted for publication 31 October 2023
Published 8 December 2023

Online at stacks.iop.org/JSTAT/2023/123202
https://doi.org/10.1088/1742-5468/ad0a94

Abstract. Using the optimal fluctuation method, we evaluate the short-time probability distribution $P(\bar{H},L,t=T)$ of the spatially averaged height $\bar{H}=(1/L)\int_0^L h(x,t=T)\,\mathrm{d}x$ of a one-dimensional interface $h(x,t)$ governed by the Kardar–Parisi–Zhang equation

$$\partial_t h=\nu\partial_x^2 h+\frac{\lambda}{2}\left(\partial_x h\right)^2+\sqrt{D}\xi\left(x,t\right)$$

on a ring of length L. The process starts from a flat interface, $h(x,t=0)=0$. Both at $\lambda\bar{H}<0$ and at sufficiently small positive $\lambda\bar{H}$ the optimal (that is, the least-action) path $h(x,t)$ of the interface, conditioned on $\bar{H}$, is uniform in space, and the distribution $P(\bar{H},L,T)$ is Gaussian. However, at sufficiently large $\lambda\bar{H}>0$ the spatially uniform solution becomes sub-optimal and gives way to non-uniform optimal paths. We study these, and the resulting non-Gaussian distribution

*Author to whom any correspondence should be addressed.

1742-5468/23/123202+30$33.00

$P(\bar{H},L,T)$, analytically and numerically. The loss of optimality of the uniform solution occurs via a dynamical phase transition of either first or second order, depending on the rescaled system size $\ell = L/\sqrt{\nu T}$, at a critical value $\bar{H} = \bar{H}_c(\ell)$. At large but finite ℓ the transition is of first order. Remarkably, it becomes an 'accidental' second-order transition in the limit of $\ell \to \infty$, where a large-deviation behavior $-\ln P(\bar{H},L,T) \simeq (L/T) f(\bar{H})$ (in the units $\lambda = \nu = D = 1$) is observed. At small ℓ the transition is of second order, while at $\ell = O(1)$ transitions of both types occur.

Keywords: large deviations in non-equilibrium systems, growth processes, fluctuation phenomena

Contents

1. Introduction

Atypically large fluctuations in macroscopic systems out of equilibrium continue to attract great interest from statistical physicists. Although a universal description of such fluctuations is unavailable, there has been much progress in studies of particular systems. One of the main theoretical tools in this area is known under different names in different areas of physics: the optimal fluctuation method (OFM), the instanton method, the weak-noise theory, the macroscopic fluctuation theory, etc. This method

J. Stat. Mech. (2023) 123202

relies on a saddle-point evaluation of the pertinent path integral of the stochastic process, conditioned on the large deviation. The method is based on a model-specific small parameter (often called 'weak noise'), and it brings about a conditional variational problem. The solution of this problem—a deterministic, and in general time-dependent, field—describes the 'optimal path' of the system: the most probable system's history that dominates the contribution of different paths to the statistics in question.

Among multiple applications of the OFM, we focus on one set of problems which has attracted attention in the last two decades [1–22]: short-time large deviations of a stochastically growing interface as described by the one-dimensional Kardar–Parisi–Zhang (KPZ) equation [23]

$$\partial_t h = \nu \partial_x^2 h + \frac{\lambda}{2} (\partial_x h)^2 + \sqrt{D}\xi(x,t), \tag{1}$$

where $\xi(x,t)$ is a white noise with

$$\langle \xi(x,t) \rangle = 0, \quad \langle \xi(x,t)\xi(x',t') \rangle = \delta(x-x')\delta(t-t'). \tag{2}$$

Here we employ the OFM to study a KPZ interface on a ring of length L, i.e. with periodic boundary conditions at $x=0$ and $x=L$. The interface is initially flat,

$$h(x,t=0) = 0, \tag{3}$$

and we are interested in evaluating the probability density function (PDF) $P\left(\bar{H},L,T\right)$ of the spatially averaged surface height

$$\bar{H} = \frac{1}{L}\int_0^L h(x,T)\,\mathrm{d}x \tag{4}$$

at a final time $t=T>0$, which is much shorter than the characteristic nonlinear time of equation (1), $\tau_{\mathrm{NL}} = \nu^5/D^2\lambda^4$. The short-time limit allows one to employ the OFM in a controlled manner [1–5, 7, 9–12, 14–20, 22], as we will reiterate shortly. The problem, defined by equations (1)–(4), continues the line of study in [10, 22] of finite system-size effects (which turn out to be quite dramatic) in large deviations of height of the KPZ interface.

Upon rescaling $t \to tT$, $x \to (\nu T)^{1/2}x$, $h \to \nu h/\lambda$ and $\xi \to \left(\nu T^3\right)^{-1/4}\xi$, equation (1) becomes

$$\partial_t h = \partial_x^2 h + \frac{1}{2}(\partial_x h)^2 + \sqrt{\varepsilon}\xi(x,t), \tag{5}$$

with rescaled noise strength $\varepsilon = D\lambda^2 T^{1/2}/\nu^{5/2}$ on a ring of rescaled length $\ell = L/\sqrt{\nu T}$. The PDF of the rescaled average height $\bar{H}$ at final time $t=1$ can then be written as a path integral

$$P\left(\bar{H},\ell,\varepsilon\right) = \int_{h(\cdot,0)=0} Dh\,\delta\left(\frac{1}{\ell}\int_0^\ell h(x,1)\,\mathrm{d}x - \bar{H}\right) J[h] \exp\left\{-\frac{1}{\varepsilon}S[h]\right\} \tag{6}$$

J. Stat. Mech. (2023) 123202

with action functional

$$S[h]=\int_0^1 \mathrm{d}t\int_0^\ell \mathrm{d}x\,\mathcal{L}(h,\partial_t h)=\frac{1}{2}\int_0^1 \mathrm{d}t\int_0^\ell \mathrm{d}x\left[\partial_t h-\partial_x^2 h-\frac{1}{2}(\partial_x h)^2\right]^2, \tag{7}$$

where $\mathcal{L}(h,\partial_t h)$ is the Lagrangian. The OFM assumes a weak-noise limit $\varepsilon\to 0$ when the path integral (6) can be evaluated by the saddle-point method, while the Jacobian $J[h]$ does not contribute in the leading-order. In this limit, the PDF $P(\bar{H},\ell,\varepsilon)$ is dominated by the optimal path of the system, that is by the most likely history $h(x,t)$, conditional on a given average height at $t=1$

$$-\ln P\left(\bar{H},\ell,\varepsilon\right)\overset{\varepsilon\to 0}{\simeq}\varepsilon^{-1}\min_{\substack{h(\cdot,0)=0,\\ \int_0^\ell h(x,1)\mathrm{d}x=\ell\bar{H}}} S[h]=\varepsilon^{-1}S\left(\bar{H},\ell\right). \tag{8}$$

Hence, the PDF can be determined, up to pre-exponential factors, from the solution of this constrained minimization problem. Here we will solve this minimization problem numerically for different $\bar{H}$ and ℓ, and analytically in the asymptotic limits of large and small ℓ.[4]

It will be convenient to present our results by setting $\nu=\lambda=D=1$.[5] Then the weak-noise scaling (8) reads

$$-\ln P\left(\bar{H},\ell,\varepsilon\to 0\right)\simeq T^{-1/2}S\left(\bar{H},\ell\right). \tag{9}$$

Note that the limit $\varepsilon\to 0$ at fixed ℓ corresponds to the short-time limit $T\to 0$ and small-length limit $L\to 0$ with $L/\sqrt{T}=\text{const}$. When instead T goes to zero at $L=\text{const}$, one has both $\varepsilon\to 0$ and $\ell\to\infty$. The latter limit turns out to be most interesting, and it is analyzed here in detail. It is natural to expect that for any $\bar{H}$, when $\ell\to\infty$, the action $S(\bar{H},\ell)$ should exhibit a large-deviation form

$$S\left(\bar{H},\ell\right)\overset{\ell\to\infty}{\simeq}\ell f\left(\bar{H}\right), \tag{10}$$

leading to

$$-\ln P\left(\bar{H},L,T\to 0\right)\simeq (L/T)\,f\left(\bar{H}\right), \tag{11}$$

and this is what we indeed observe here. Less expectedly, we also find that the rate function $f(\bar{H})$ exhibits, at a critical value $\bar{H}=\bar{H}_{\mathrm{c}}(\ell)$, a dynamical phase transition (DPT) which is *accidentally* second-order. By that we mean that the rate function at the critical point becomes continuously differentiable *only* in the limit of $\ell\to\infty$. At arbitrary large but finite ℓ the large-deviation form (10) breaks down. We show, however, that the action $S(\bar{H},\ell)$ still exhibits a DPT at a critical point $\bar{H}=\bar{H}_{\mathrm{c}}$, but this DPT is of (weakly) first order and the optimal path at the critical point changes discontinuously via a subcritical bifurcation.

[4] Note that whenever there exists a spatially non-uniform optimal path there are actually infinitely many possible paths due to the translational symmetry of the problem with respect to x. Accounting for this submanifold of degenerate solutions and for the associated zero mode is, however, only relevant for pre-exponential factors [22], which we do not address here.

[5] In most of the paper we assume, without loss of generality, that $\lambda>0$. Indeed, changing λ to $-\lambda$ is equivalent to changing h to $-h$.

J. Stat. Mech. (2023) 123202

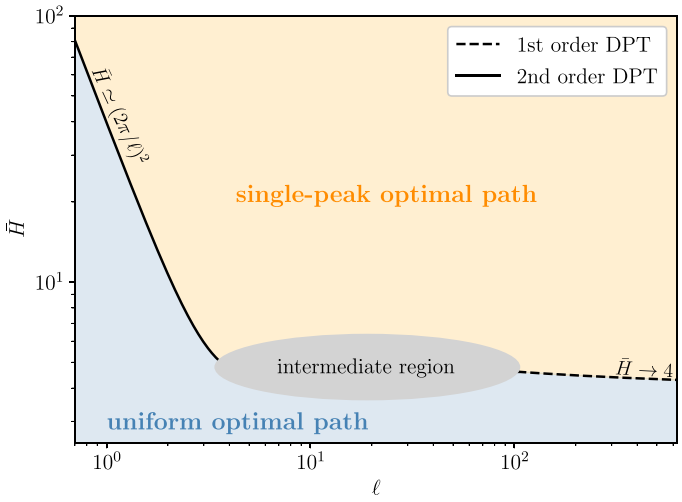

Figure 1. An overview of our main results for the large-deviation problem (8) on the $(\bar{H},\ell)$ phase diagram. In the light blue region, which extends to all $\bar{H}<0$, the global minimum of the action functional (7) is attained at the spatially uniform solution (19). In the light orange region, the least-action solution $h(x,t)$ is instead a spatially non-uniform path with a single maximum. For small domain sizes $\ell \to 0$ it is given by equation (67), and for large domain sizes it is described in section 5.1. For small ℓ, there is a second-order DPT from the uniform to the peaked solution, as discussed in sections 3 and 6. For large ℓ, a (weakly) first-order transition takes place instead, at $\bar{H}$ approximately given by equation (64). In the intermediate region transitions of both first and second order occur. Here some numerical results are available, see figure 7, but a complete understanding is lacking.

For small ℓ a truly second-order DPT is observed as predicted earlier [10, 22]. At intermediate values of $\ell = O(1)$ DPTs of both types occur. In the latter regime analytical results are unavailable as of yet, and we present some numerical results. All the DPTs that we found in this system occur because of a loss of optimality of a path that is uniform in space. The loss of optimality takes the form either of a subcritical bifurcation (for the first-order DPTs), or a supercritical bifurcation (for the true second-order DPTs). We summarize our main results on the $(\bar{H},\ell)$ phase diagram of the system in figure 1.

The remainder of this paper is structured as follows. In section 2 we formulate the OFM equations and boundary conditions, present a simple uniform solution of these equations, previously studied in [10, 22], and argue that it describes the optimal path of the system at all $\lambda H<0$. Supercritical bifurcations of the uniform solution have recently been studied in [22]. Still, for convenience of further discussion, we briefly rederive them in section 3. Section 4 includes our results of numerical minimization of the action functional (7) in different regions of the $(\bar{H},\ell)$ phase diagram. These numerical results provided valuable insights into the nature of optimal paths of the interface which led us to develop asymptotic analytical solutions of the OFM problem for large ℓ that we present in section 5. The asymptotic solution for small ℓ is briefly discussed in section 6.

J. Stat. Mech. (2023) 123202

We summarize and discuss our main results in section 7. A description of the numerical algorithms that we use here is relegated to the appendix.

2. OFM equations and uniform solution

At a technical level, the main objective of this work is to determine the minimum action $S(\bar{H},\ell)$ as a function of the rescaled average height $\bar{H}$ and rescaled system size ℓ. In this section, we present the necessary conditions for minimizers of the action functional (7), namely the OFM equations and the boundary conditions. We argue then that a simple spatially uniform solution of the ensuing OFM problem is always optimal for $\bar{H}<0$.

The first-order necessary conditions for a minimizer of the action functional (7) can be represented as a pair of Hamilton's equations for the optimal history of the interface $h(x,t)$ and the conjugate momentum density $p=\partial\mathcal{L}/\partial(\partial_t h)$. These equations have been derived in many papers [1–5, 7, 9–12, 14–20, 22], and they take the form

$$\partial_t h = \partial_x^2 h + \frac{1}{2}(\partial_x h)^2 + p, \tag{12}$$

$$\partial_t p = -\partial_x^2 p + \partial_x (p\partial_x h). \tag{13}$$

The 'momentum density' $p(x,t)$ describes the (rescaled) optimal realization of the external noise $\xi(x,t)$ that drives the interface conditional on a specified $\bar{H}$. In the present case equations (12) and (13) should be complemented by the periodic boundary conditions at $x=0$ and $x=\ell$, by the initial condition

$$h(x,0)=0, \tag{14}$$

and by the final-time condition

$$p(x,1)=\Lambda=\text{const}, \tag{15}$$

which follows from the demand that a boundary term at $t=1$, originating from an integration by parts, should vanish for any $h(x,1)$. The parameter Λ is a Lagrange multiplier which needs to be chosen so as to impose the rescaled final-time condition

$$\frac{1}{\ell}\int_0^\ell h(x,1)\,\mathrm{d}x = \bar{H}. \tag{16}$$

Once the optimal path is determined, the action $S(\bar{H},\ell)$ can be determined from the equation

$$S=\frac{1}{2}\int_0^1 \mathrm{d}t \int_0^\ell \mathrm{d}x\, p^2(x,t), \tag{17}$$

which follows from equations (7) and (12).

J. Stat. Mech. (2023) 123202

By differentiating the action $S(\bar{H},\ell) = S[h(x,t;\bar{H},\ell)]$ of the optimal profile $h = h(x,t;\bar{H},\ell)$ with respect to $\bar{H}$ using the chain rule, one can show that Λ is related to the action via

$$\Lambda = \frac{1}{\ell}\frac{\partial S\left(\bar{H},\ell\right)}{\partial \bar{H}} \quad \left(\text{or } \mathrm{d}S = \ell\Lambda \mathrm{d}\bar{H}\right). \tag{18}$$

If the action $S(\bar{H},\ell)$ is a strictly convex function of $\bar{H}$, there is a bijective relation between Λ and $\bar{H}$, and it suffices, for the purpose of calculating the action, to only determine $\bar{H}(\Lambda)$ and use equation (18). This shortcut is very convenient and holds for many large-deviation calculations [24].

There is an obvious exact solution of the OFM equations and the boundary conditions

$$h\left(x,t\right) = \bar{H}t, \qquad p\left(x,t\right) = \Lambda, \qquad \Lambda = \bar{H}, \qquad S = \frac{\ell}{2}\bar{H}^2, \tag{19}$$

that describes a uniformly growing flat interface. We will often call this branch of solutions branch 1. By virtue of equation (8), whenever the uniform solution (19) is the optimal one, we have a Gaussian PDF for $\bar{H}$ up to pre-exponential factors. Of most interest, however, are the regions of parameters $\bar{H}$ and ℓ, for which the uniform solution is sub-optimal. As we will see, the loss of optimality can occur via either a supercritical or a subcritical bifurcation.

First of all, we can argue that, for negative $\bar{H}$, the uniform solution (19) is always optimal. Using the evident conservation law

$$\frac{1}{\ell}\int_0^\ell p\left(x,t\right)\mathrm{d}x = \Lambda = \text{const} \tag{20}$$

of equation (13), we can rewrite the action (7) for any solution of the OFM equations as

$$S = \frac{1}{2}\int_0^1 \mathrm{d}t \int_0^\ell \mathrm{d}x\, p^2\left(x,t\right) = \ell\frac{\Lambda^2}{2} + \frac{1}{2}\int_0^1 \mathrm{d}t \int_0^\ell \mathrm{d}x\left[p\left(x,t\right) - \Lambda\right]^2. \tag{21}$$

Also, integrating both sides of equation (12) with respect to t from 0 to 1 and with respect to x over the ring, and using the periodic boundary conditions and the conservation law (20), we obtain

$$\bar{H} = \frac{1}{\ell}\int_0^\ell h\left(x,1\right)\mathrm{d}x = \Lambda + \frac{1}{2\ell}\int_0^1 \mathrm{d}t \int_0^\ell \mathrm{d}x\left[\partial_x h\left(x,t\right)\right]^2. \tag{22}$$

One can easily see from equations (21) and (22) that at negative Λ (or $\bar{H}$) any inhomogeneity in the momentum density p both increases the action S and decreases the average height $|\bar{H}|$ compared with their values for the uniform solution. Therefore, any nonuniform solution here is sub-optimal.

J. Stat. Mech. (2023) 123202

In contrast to this, for $\Lambda > 0$ (or $\bar{H} > 0$) an inhomogeneity increases both S and $\bar{H}$ compared with the uniform solution. A competition between these two opposite effects may give rise to non-uniform solutions with lesser action than the uniform one, as we will indeed see in the following.

3. Bifurcations of the uniform solution

In this brief section we carry out a linear stability analysis of the uniform solution (19). We find that, for sufficiently large positive $\bar{H}$, the uniform solution can continuously and supercritically bifurcate to a non-uniform solution. The first spatial Fourier mode to become unstable as $\bar{H}$ increases depends on the rescaled system size ℓ in a nontrivial way and is determined from equation (26). This equation was also obtained in [22] by calculating the leading-order prefactor correction to the asymptotic scaling in equation (8) through Gaussian integration of fluctuations around the uniform solution (19).

At first order of a perturbation theory around the uniform solution (19) we have

$$p(x,t) = \bar{H} + b(t)\cos qx, \qquad h(x,t) = \bar{H}t + a(t)\cos qx, \qquad |a|, |b| \ll 1. \tag{23}$$

Here the wave number q spans the set $2\pi m/\ell$ for $m = 1, 2, \ldots$. Substituting the expressions (23) into equations (12) and (13) and neglecting higher-order terms, we obtain the following system of linear ordinary differential equations:

$$\dot{a} = -q^2 a + b, \qquad \dot{b} = q^2 b - q^2 \bar{H} a. \tag{24}$$

It has solutions proportional to $\mathrm{e}^{\mathrm{i}\omega t}$, where

$$\omega = \pm q\sqrt{\bar{H} - q^2}. \tag{25}$$

Using the boundary conditions (14) and (15), we obtain the following relationship between q and $\bar{H} = \bar{H}_{\mathrm{c}}(q)$ at the bifurcation points:

$$\tan\left(q\sqrt{\bar{H} - q^2}\right) = -\frac{\sqrt{\bar{H} - q^2}}{q}. \tag{26}$$

Note that the trivial solution $\bar{H} = q^2$ of equation (26) does not correspond to a valid non-uniform solution due to the boundary conditions at $t = 0$ and 1. The resulting dependence $\bar{H}(q)$ can be expressed in a parametric form

$$\bar{H} = -\frac{2u}{\sin 2u}, \qquad q = \sqrt{-u\cot u}, \qquad \frac{(2n-1)\pi}{2} < u < n\pi; \quad n = 1, 2, 3, \ldots, \tag{27}$$

where, for given ℓ, only values of $q = 2\pi m \ell^{-1}$ with $m = 1, 2, 3, \ldots$ are allowed. The first three branches of equation (27) are shown in figure 2. As one can see, the first instability appears for $n = 1$, and a necessary condition for the instability, for any ℓ, is $\bar{H}_{\mathrm{c}} \geqslant 4.603$. When $\ell \to \infty$, the first instability of the uniform solution will occur, at $\bar{H}_{\mathrm{c}} \simeq 4.603$, for a very high mode $m \simeq 1.343\,\ell/2\pi$. For finite ℓ, one can find the bifurcation point on the $n = 1$ branch of equation (27) numerically. Finally, for $\ell \to 0$, the first instability occurs for the $m = 1$ mode at $\bar{H} \simeq (2\pi/\ell)^2$ in agreement with [10].

J. Stat. Mech. (2023) 123202

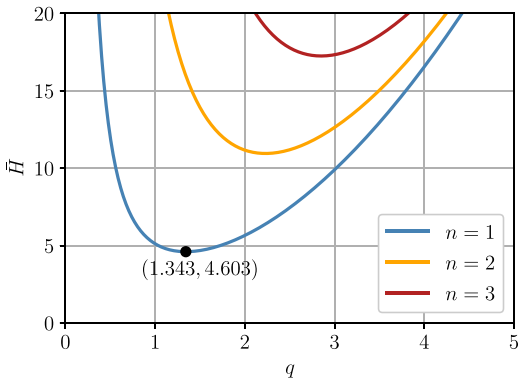

Figure 2. The supercritical bifurcation points $\bar{H} = \bar{H}_c$ versus the wave number q as predicted by equation (27) for $n = 1, 2$ and 3. Only discrete values of $q = 2\pi m \ell^{-1}$ with $m = 1, 2, \ldots$ are allowed. The lowest curve corresponds to $n = 1$. The black dot indicates the global minimum of $\bar{H}_c$ versus q, so that $\bar{H}_c \geqslant 4.603$ is a necessary condition for a supercritical bifurcation of the uniform solution for any ℓ.

4. Numerical results

Now we proceed with a numerical solution of the minimization problem in equation (8) for different $\bar{H}$ and ℓ. The numerical methods that we used are described in the appendix. In addition to confirming the supercritical bifurcations of the uniform solution that we discussed in section 3, we will uncover important subcritical bifurcations and gain insight into non-perturbative optimal paths which will be studied analytically in sections 5 and 6.

We start with the simpler case of small ℓ. Choosing a moderately small value $\ell = \pi/8$ and numerically minimizing the action (A1) for different Λ, we obtain the rate function $S(\bar{H}, \ell)$ and Lagrange multiplier $\Lambda(\bar{H})$ shown in figure 3. The spatially uniform solution (19), corresponding to branch 1 of the action, is seen to become unstable close to $\bar{H} \simeq (2\pi/\ell)^2$, as stated in section 3, and there is a continuous (second-order) DPT to a spatially nonuniform solution. Indeed, the $(m = 1)$-spatial Fourier mode of the profile becomes unstable at this point. One such spatially nonuniform solution close to the transition point is shown in figure 4. As $\bar{H}$ increases, the optimal solution turns, for most of the time $0 < t < 1$, into a stationary 'cnoidal' solution for p which drives an h-profile that is non-uniform in x but is uniformly translating in the vertical direction. The same solution appears in the problem of the one-point height distribution for the KPZ equation on a ring [10], and we use it in section 6 to calculate the theoretical curves in figures 3 and 4, which match the numerical results quite well.

Next, we turn to the more complicated and interesting case of large ℓ. For $\ell = 16\pi$ the minimization of the augmented action (A2) leads to the results for the rate function $S(\bar{H})$ and Lagrange multiplier $\Lambda(\bar{H})$ shown in figure 5. In addition to branch 1 we observe two other branches of solutions. Branch 2 is observed to the right of a narrow transition region close to $\bar{H} \simeq 4$. On this branch the action $S(\bar{H})$ is approximately a linear function while Λ is almost constant. Further, for much larger $\bar{H}$, there

J. Stat. Mech. (2023) 123202

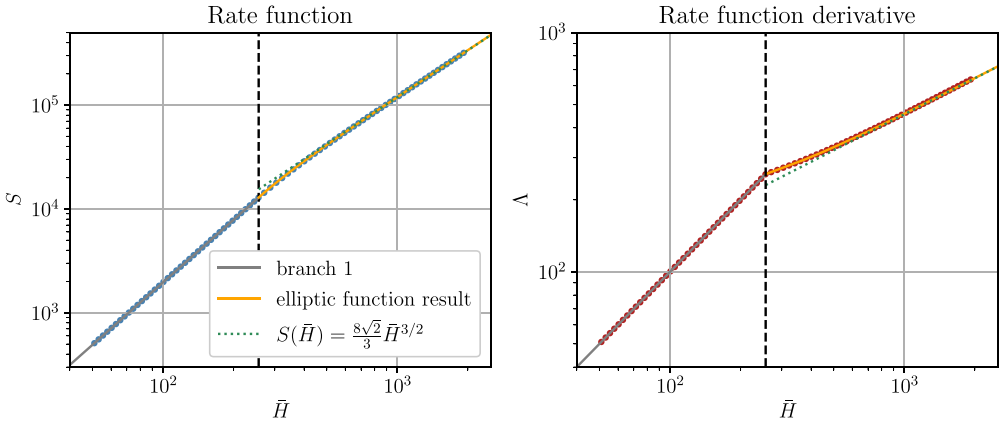

Figure 3. Comparison of analytical small-ℓ results (lines) and numerics (dots) for the rate function $S(\bar{H})$ (left) and Lagrange multiplier $\Lambda(\bar{H})$ (right) for a rescaled system size of $\ell = \pi/8$. The numerical computations were performed at resolutions $n_x = 64$ and $n_t = 8000$. The dashed vertical line indicates where the spatially uniform solution becomes unstable at $\bar{H} \simeq 256.04$ in agreement with equation (26). The dotted green line corresponds to the asymptotic $S(\bar{H}) = (8\sqrt{2}/3)\,\bar{H}^{3/2}$ (see equation (73)), the gray line corresponds to the spatially uniform solution (19) and the orange line corresponds to equations (70) and (72).

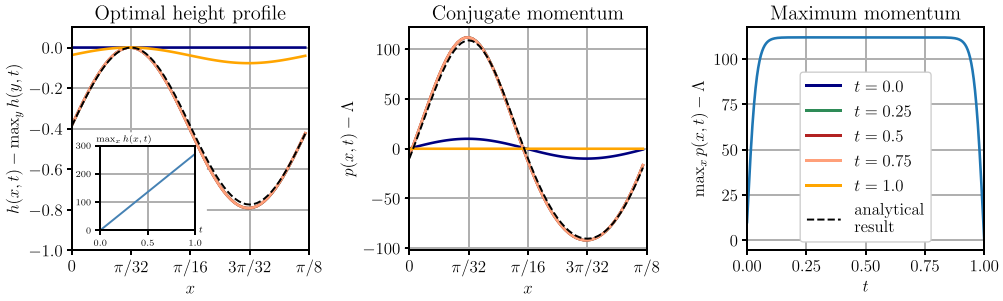

Figure 4. Numerically found spatially slightly non-uniform solution of equations (12) and (13) for $\bar{H} = 270.319$ and a moderately small rescaled system size of $\ell = \pi/8$ with numerical resolutions $n_x = 64$ and $n_t = 8000$. The numerically found action $S = 14322.081$ deviates by 0.009% from the predicted small-ℓ result $S = 14320.806$ for this $\bar{H}$ as given by equation (70). The action for the spatially uniform solution (19) for the same $\bar{H}$ and ℓ would be $S = 14347.685$. The maximum height at final time is $H = 270.357$. Left: optimal height profile $h(x,t)$ at different times t, with the maximum at each t subtracted in order to emphasize deviations from spatial homogeneity. The prediction (67) for intermediate times is indicated by the black dashed line and agrees well with the numerical solutions for $t = 0.25$, $t = 0.5$ and $t = 0.75$. The inset shows that the growth of the maximum $\max_x h(x,t)$ in time is still linear as predicted. Center: conjugate momentum density $p(x,t)$ with $\Lambda = 261.057$ subtracted, compared with the analytical result (68) indicated by the black dashed line. Right: spatial maximum $\max_x p(x,t)$ over time to visualize the long lifetime of the stationary cnoidal solution with some small boundary layers in time at $t = 0$ and $t = 1$.

J. Stat. Mech. (2023) 123202

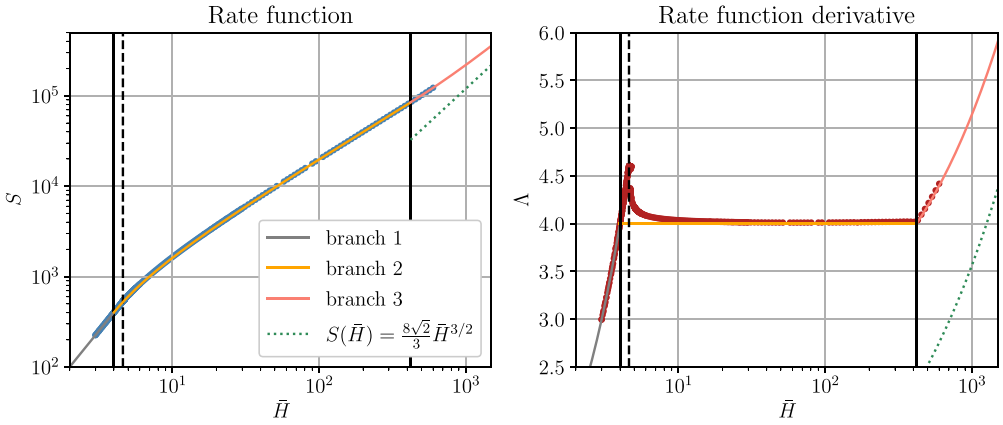

Figure 5. Analytical large-ℓ results of section 5 (lines) versus numerics (dots) for the rate function $S(\bar{H})$ (left) and Lagrange multiplier $\Lambda(\bar{H})$ (right) for a rescaled system size of $\ell = 16\pi$. The numerical computations were performed at resolutions $n_x = 1024$ and $n_t = 4000$. The analytically found branches for the action $S(\bar{H})$ and Lagrange multiplier $\Lambda(\bar{H})$ at large ℓ are drawn as colored lines according to the results summarized in equation (31), with $\Lambda(\bar{H})$ then obtained from equation (18). The solid vertical lines indicate the theoretical critical points in the large-ℓ limit at $\bar{H} \simeq 4$ and $\bar{H} \simeq \ell^2/6$. The dashed vertical line shows where the spatially uniform solution becomes unstable in the $(m = 11)$ spatial Fourier mode, as given by the minimization of equation (27) over the allowed wave numbers. The dotted green line corresponds to the asymptotic behavior $S(\bar{H}) = (8\sqrt{2}/3)\bar{H}^{3/2}$ (see equation (58)). A better resolved transition region close to $\bar{H} = 4$ is shown in figure 7.

is a smoothed-out second-order transition from branch 2 to a third branch 3 with a different scaling behavior. The optimal paths for branches 2 and 3 are shown in figure 6. They consist of strongly localized large-amplitude stationary solitons of p that drive an outgoing almost triangular structure of h (or two antishocks of $V(x,t) = \partial_x h(x,t)$, see section 5). The solution, corresponding to branch 2, clearly emerges via a subcritical, rather than supercritical, bifurcation. Strikingly, the soliton has a well-defined lifetime which is very close to 1/2. The difference between branches 2 and 3 is that, for branch 3, the two edges of the triangular structure of $h(x,t)$ collide before the final time $t = 1$ is reached, while for branch 2 they do not.

These crucial findings will guide our stationary-soliton-based asymptotic theory for large ℓ that we develop in section 5. There we give an analytical description of the optimal paths for branches 2 and 3, which are the only relevant ones for large ℓ. There we establish a first-order transition at $\bar{H} \simeq 4$ for large but finite ℓ and show that it becomes 'accidentally' second order in the limit of $\ell \to \infty$. We also find that the smoothed-out second-order transition from branch 2 to branch 3 occurs at $\bar{H} = \ell^2/6$. The resulting analytical predictions, indicated by the lines in figures 5 and 6, are in good agreement with numerics at large, but finite, ℓ.

At moderate ℓ the transition region where the spatially uniform solution (19) of branch 1 becomes sub-optimal is quite complex, as one can appreciate from figure 7. We see that, in general, there are both first- and second-order transitions in this region:

J. Stat. Mech. (2023) 123202

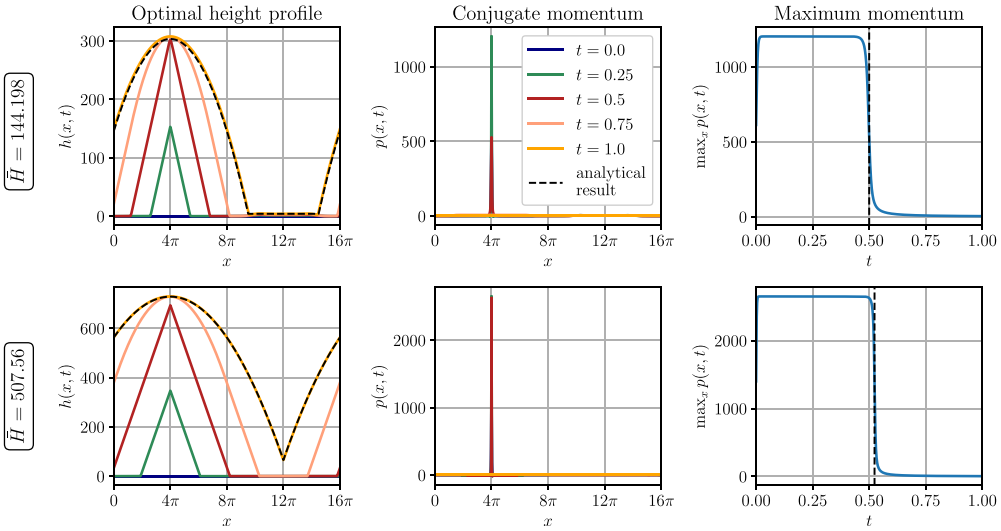

Figure 6. Numerically found least-action solutions of equations (12) and (13) for two mean heights $\bar{H} = 144.198$ (top row) and $\bar{H} = 507.56$ (bottom row) at $\ell = 16\pi$ with numerical resolutions $n_x = 2048$ and $n_t = 4000$. Both solutions are one-soliton solutions for branches 2 and 3, respectively. The action of the solution in the top row is $S = 28\,723.766$, which deviates by 0.4% from the predicted large-ℓ result $S = 28\,590.660$ given by equation (50). The action for the bottom row solution is $S = 102\,754.528$, so it deviates by 0.2% from the predicted value $S = 102\,522.498$ for this mean height given by equation (56). The qualitative difference of these solutions is whether the two edges of the growing triangle for h collide. The left column shows the optimal height profile $h(x,t)$ at different times t, together with the predictions (44), (45) and (55) for the final time $t = 1$. The center column shows the corresponding conjugate momentum density $p(x,t)$. The right column shows the spatial maximum $\max_x p(x,t)$ over time to visualize the lifetime of the stationary soliton solution and compare it with the analytical expressions $\tau = 1/2$ for branch 2 and equation (59) for branch 3 (dashed vertical lines).

the uniform solution becomes linearly unstable for some $m > 1$, leading to second-order transitions, but there is also a competition with the (subcritical) one-soliton solution. The subcritical scenario clearly wins for sufficiently large ℓ. Indeed, for $\ell = 32\pi$ we observe only a first-order transition from the spatially uniform to the soliton solution, while the linear instability becomes irrelevant.

Note that, for branch 2, in addition to stationary single-soliton solutions of the OFM equation discussed so far, there are also stationary multi-soliton solutions consisting of two or more (almost) non-interacting strongly localized stationary solitons of p and corresponding expanding triangles of h. One such solution, which we observed numerically, is shown in the top row of figure 8. We found, however, that such solutions always have a larger action than the one-soliton solution for the same ℓ and $\bar{H}$. Therefore, the one-soliton solution indeed seems to provide the optimal solution. In the limit $\ell \to \infty$, these multi-soliton solutions—a soliton gas—would contribute to the pre-exponential factor for $\mathcal{P}(\bar{H}, \ell)$, but pre-exponential factors are beyond the scope of this paper. Additionally,

J. Stat. Mech. (2023) 123202

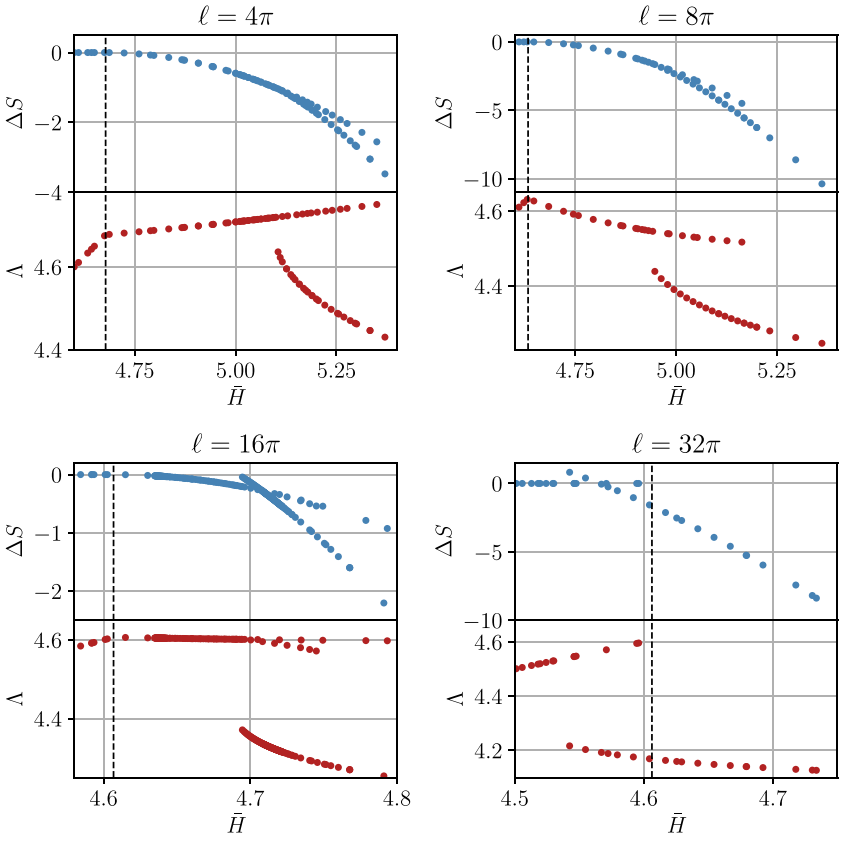

Figure 7. Numerically computed action $S(\bar{H})$ and Lagrange multiplier $\Lambda(\bar{H})$ for different ℓ in the transition region not far from $\bar{H} = 4$, where the transition between branches 1 and 2 at large ℓ is predicted (see equation (31)). Using the numerical minimization techniques described in the appendix, we search for (possibly multiple distinct local) minimizers of the action functional (7) for given ℓ and $\bar{H}$. When there is more than one minimizer for the same ℓ and $\bar{H}$, the one with the least action gives the true optimal solution. For a better visualization we show the difference between the numerically computed action of the found solutions and the action $\ell\bar{H}^2/2$ of the spatially uniform solution. The vertical dashed lines indicate the smallest $\bar{H}$ where a spatial Fourier mode $q = 2\pi m\ell^{-1}$ of the uniform solution first becomes unstable according to equation (27) ($m = 3$ for $\ell = 4\pi$, $m = 5$ for $\ell = 8\pi$, $m = 11$ for $\ell = 16\pi$, and $m = 21$ for $\ell = 32\pi$). For $\ell = 4\pi$, 8π and 16π, the rate function displays both a second-order transition at the predicted point and a first-order transition at slightly larger $\bar{H}$ where the one-soliton solution (see the top row of figure 6), described theoretically in section 5.2, becomes optimal. At the largest $\ell = 32\pi$, only a first-order transition from the uniform to the one-soliton solution is observed, while oscillating solutions are irrelevant. (See section 5.4 for a more detailed analysis of the transition region at large but finite ℓ.) Note that for $\ell = 16\pi$ one can also see, around $\bar{H} = 4.7$, another oscillating solution with a second superimposed wave number. The following numerical resolutions were used: $n_x = 128$ and $n_t = 2000$ for $\ell = 4\pi$, $n_x = 512$ and $n_t = 4000$ for $\ell = 8\pi$, $n_x = 1024$ and $n_t = 4000$ for $\ell = 16\pi$, and $n_x = 2048$ and $n_t = 4000$ for $\ell = 32\pi$.

J. Stat. Mech. (2023) 123202

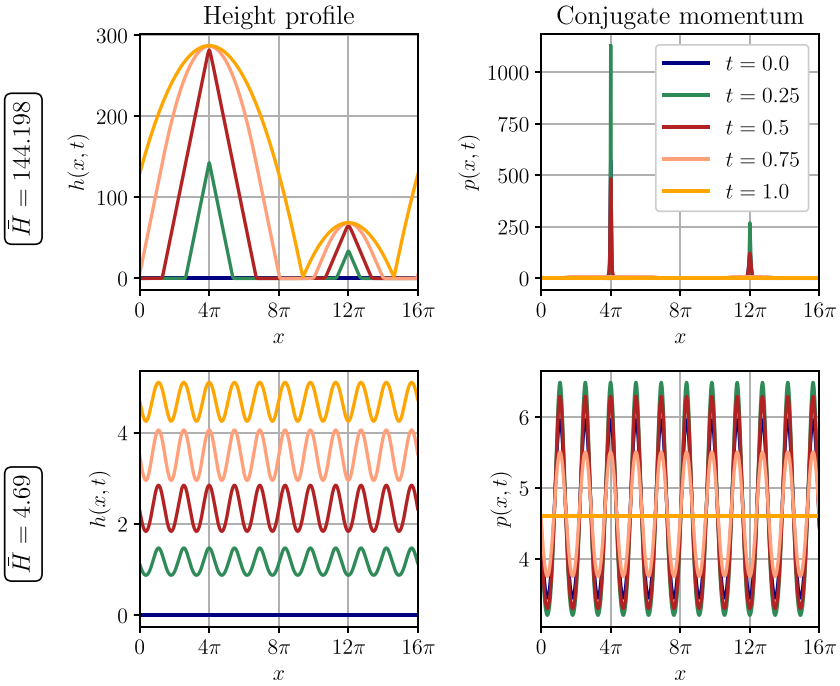

Figure 8. Two types of sub-optimal solutions to equations (12) and (13) for $\ell = 16\pi$. The top row (obtained with resolution $n_x = 2048$ and $n_t = 4000$) shows a two-soliton solution for the same value of $\bar{H} = 144.198$ as in the top row of figure 6. The action of the two-soliton solution, $S = 28\,746.682$, is larger than that for the one-soliton solution for the same ℓ and $\bar{H}$. The bottom row shows a spatially oscillating solution, originating from linear instability of the $m = 11$ mode of the spatially uniform solution for $\bar{H} \gtrsim 4.607$ as predicted by equation (27). Here the resolutions are $n_x = 1024$ and $n_t = 4000$. As can be seen from figure 7 (bottom left), this family of solutions can be optimal for small $\bar{H}$ and moderate ℓ, but it becomes irrelevant as large ℓ.

in the bottom row in figure 8, we show an optimal path for $\ell = 16\pi$ and close to $\bar{H} = 4$, which emerges through linear instability of the $(m = 11)$-mode. Later on, however, it is overtaken by the one-soliton solution.

5. Large-ℓ asymptotics: rise and fall of the soliton

5.1. General description of the solution

Guided by our numerical solutions and by previous works on the one-point KPZ height statistics on the line [4] and on a ring [10], here we find approximate asymptotic solutions of equations (12)–(15) which give rise to two nontrivial branches (we call them branches 2 and 3) of the large-deviation function $S(\bar{H})$ for large ℓ. As we found, for both branches the maximum one-point height of the interface $H = \max h(x, t = 1)$ turns out to be very large: $H \gg 1$. Therefore, in addition to the strong inequality $\ell \gg 1$ we can also use the strong inequality $H \gg 1$. This allows us to construct 'inviscid' asymptotic solutions

J. Stat. Mech. (2023) 123202

in different regions of space, separated by discontinuities of proper types. Like their numerical counterparts, the analytical solutions exhibit two distinct stages in time, with an abrupt transition between them at some branch-dependent intermediate time $0 < t = \tau < 1$, which we will determine.

For $0 < t < \tau$ the solution has the form of a strongly localized stationary soliton of $p(x,t)$ and 'antishock' of $V(x,t) = -\partial_x h(x,t)$ which were previously identified in the problem of one-point height statistics on the line [4, 5] and on a ring [10]. The characteristic width, $O(1/\sqrt{H})$, of the soliton–antishock structure is much less than unity. Outside of the soliton–antishock one has $p(x,t) \simeq 0$. As a result, equation (13) is obeyed trivially and, at distances $\gtrsim 1$ from the soliton, $h(x,t)$ follows the deterministic KPZ dynamics

$$\partial_t h = \partial_x^2 h + \frac{1}{2}(\partial_x h)^2, \tag{28}$$

which is equivalent to the Burgers equation

$$\partial_t V + V\partial_x V = \partial_x^2 V \tag{29}$$

for the field $V(x,t) = -\partial_x h(x,t)$. In addition, the diffusion term in equation (29) can also be neglected at large distances [4], and one arrives at the inviscid Hopf equation

$$\partial_t V + V\partial_x V = 0. \tag{30}$$

The stationary soliton–antishock structure drives an almost triangular configuration of $h(x,t)$ that is expanding outwards [4]. The height of the triangle grows linearly with time, while its two edges propagate with a constant speed as 'ordinary' shocks of $V(x,t)$ obeying equation (29) or, when treated as discontinuities, obeying equation (30) [4]. The positions of these shocks at $t = 1$ determine the boundaries of the 'impact region' of the soliton–antishock structure. When the size of the impact region, which scales as $O(\sqrt{H})$ [4], is shorter than the rescaled system size ℓ (this happens when $\bar{H}$ is not too large, see below), there is also an external region where the uniform solution $p(x,t) = \Lambda = \text{const}$ and $V(x,t) = 0$ holds (see equation (19)). The external uniform solution holds for all times $0 < t < 1$, and it contributes to the large-deviation function of $\bar{H}$. In the inviscid limit the regions of zero and nonzero p are divided by a stationary discontinuity. This regime corresponds to branch 2.

Branch 3 appears when, due to the periodicity of the system, the ordinary shocks of $V(x,t)$ collide with each other before the final time $t = 1$ is reached. In this case the impact region of the soliton–antishock structure extends to the whole system, and a region with a uniform solution does not appear.

For the solution to obey the boundary condition (15), the p-soliton must turn into a constant $p = \Lambda$ at $t = 1$. Remarkably, as we have seen in our numerical results for large ℓ, the soliton rapidly decays in the vicinity of a well-defined time $t = \tau < 1$. For both branches 2 and 3, the subsequent dynamics, at $\tau < t < 1$, gives only a subleading contribution (which we neglect, alongside other subleading contributions) to the maximum one-point height H and to the action. This stage is important, however, for determining $\bar{H}$. We can qualitatively understand this nontrivial temporal structure of the solutions

J. Stat. Mech. (2023) 123202

from the viewpoint of action minimization: first, for $0 \leqslant t \leqslant \tau$, the interface is efficiently driven upward by a stationary p-soliton, in the same manner as for the one-point height PDF of the KPZ equation on the line [4] and on a ring [10]. Then, quickly suppressing the soliton at an intermediate time $0 < \tau < 1$ and evolving the interface according to the almost free KPZ dynamics for $\tau < t \leqslant 1$ increases considerably the average height $\bar{H}$ for a negligible additional cost in terms of action. The optimal value of τ is the one that minimizes the action for a given $\bar{H}$.

As an overview, we present here the action $S(\bar{H},\ell)$ at leading order for large ℓ, as will be derived in sections 5.2 and 5.3:

$$S\left(\bar{H},\ell\right) \simeq \begin{cases} \frac{\bar{H}^2}{2}\ell, & -\infty < \bar{H} \leqslant 4, \quad \text{(branch 1)} \\ \left(4\bar{H}-8\right)\ell, & 4 < \bar{H} \leqslant \frac{\ell^2}{6}, \quad \text{(branch 2)} \\ \bar{H}^{3/2}\Phi\left(\bar{H}/\ell^2\right), & \frac{\ell^2}{6} < \bar{H} < \infty, \quad \text{(branch 3)} \end{cases} \tag{31}$$

where the function $\Phi(\ldots)$ is defined in equation (57) and obeys $\Phi(z \to \infty) \to 8\sqrt{2}/3$. The first line in equation (31) comes from the uniform solution (19). The first two lines manifestly reveal the large-deviation scaling (11), while the third line does not.

Now we proceed to a more detailed description of the solutions, and we will start with branch 2.

5.2. Branch 2

Due to a translational symmetry of the problem (12)–(15), we can place the soliton–antishock structure at $x = 0$ (see figure 9) so that, to the leading order, $H \simeq h(0,\tau)$. As explained above, at $H \gg 1$, the p-soliton can be considered as a point-like object. We will only need the value of its 'mass', $\int \mathrm{d}x\, p(x,t)$ which, by virtue of equation (13), is conserved. Using the explicit expression for the soliton, $p(x,t) = p_s(x) = 2c\cosh^{-2}(\sqrt{c/2}\,x)$ [4], where $c = H/\tau$, we obtain

$$\int_{-\infty}^{\infty} \mathrm{d}x\, p_s\left(x\right) = \sqrt{\frac{32H}{\tau}}. \tag{32}$$

The base of the triangular structure of the h-profile is equal to

$$2a\left(t\right) = \sqrt{\frac{2H}{\tau}}\,t, \tag{33}$$

while the triangle's height is

$$h\left(0,t\right) = \frac{Ht}{\tau}, \quad 0 < t < \tau. \tag{34}$$

Let us denote the total size of the impact region of the soliton–antishock structure by $2a_1$, where $a_1 \equiv a(t=1)$. In the region $a(t) < |x| < a_1$ we have

$$p = h = 0. \tag{35}$$

J. Stat. Mech. (2023) 123202

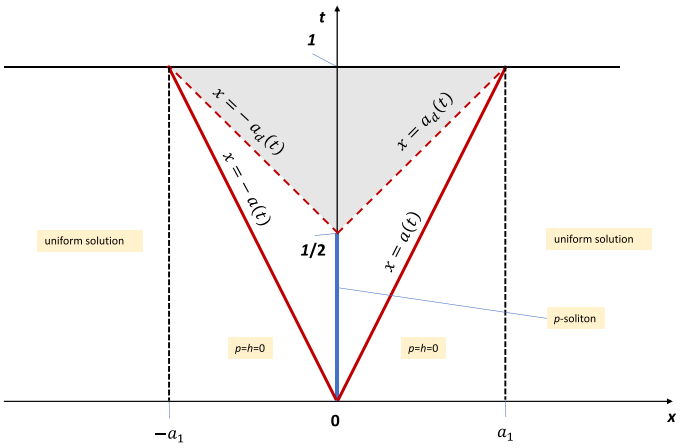

Figure 9. A space–time map of the optimal path of the system which determines the large-deviation function $S(\bar{H})$ of branch 2 in the large-ℓ limit. The thick blue line shows the position of the stationary p-soliton and V-antishock. The thick red lines show the positions of propagating ordinary shocks (see equation (33)). The dashed red lines show the positions of propagating weak discontinuities caused by the rapid decay of the p-soliton at $t=\tau=1/2$ (see equation (42)). The weak discontinuities catch up with the (twice as slow) ordinary shocks at $t=1$. This condition selects $\tau=1/2$. The boundaries of the impact region of the soliton–antishock are shown by the dashed black lines. Outside the impact region, the uniform solution (45) holds. The regions between the dashed black lines and the thick dark lines correspond to the trivial solution (35). In the regions between the dashed and thick red lines, there remain linear h-profiles of the original 'triangular solution' (see equation (36)). Inside the gray triangle the solution is described by equations (40) and (41), leading to equation (44).

The triangular profile of h on the interval $0<|x|<a(t)$ is described by the expressions [4]

$$p(x,t)=0, \quad h(x,t)=H\left(\frac{t}{\tau}-\frac{\sqrt{2}|x|}{\sqrt{H\tau}}\right) \quad \text{and} \quad V(x,t)=-\partial_x h(x,t)=\tilde{V}\operatorname{sign} x, \tag{36}$$

where

$$\tilde{V}=\sqrt{\frac{2H}{\tau}}. \tag{37}$$

As one can see from equations (33) and (37), the ordinary shocks propagate with speed $\tilde{V}/2$, as to be expected from equations (29) or (30) [25].

After the rapid decay of the soliton at $t=\tau$, the 'post-soliton' solution (in the region to be determined) can be described by the ideal hydrodynamic equations corresponding to the inviscid limit of equations (12) and (13)

J. Stat. Mech. (2023) 123202

$$\partial_t V + V\partial_x V = -\partial_x p, \tag{38}$$

$$\partial_t p + \partial_x (pV) = 0. \tag{39}$$

The V-antishock now plays the role of a discontinuity which undergoes a decay starting from $t=\tau$. In the leading order we can neglect the $-\partial_x p$ term, so that equation (38) becomes the Hopf equation (30). Its solution is

$$V(x,t) = \frac{x}{t-\tau}. \tag{40}$$

Plugging equation (40) into equation (39) and using the 'final' condition (15) on $p(x,t=1)$, we obtain

$$p(x,t) = \frac{\Lambda(1-\tau)}{(t-\tau)}. \tag{41}$$

The solutions (40) and (41) hold at $t>\tau$ and $|x| \leqslant a_d(t)$. The boundaries of this region,

$$x = \pm a_d(t) \equiv \tilde{V}(t-\tau), \tag{42}$$

represent weak discontinuities, moving with the speed $\tilde{V}$, i.e. twice as fast as the ordinary shocks at $x=\pm a(t)$ (see equation (33)). Our simulations show that the weak discontinuities catch up with the shocks at $t=1$. The corresponding condition can be written as $a_d(1)=a_1$, and it yields $\tau = 1/2$.[6]

Therefore, during the second stage of the dynamics, $1/2<t<1$, $V(x,t)$ is described by the following expressions:

$$V(|x| \leqslant a_d(t), t) = \frac{x}{t-1/2}, \quad V(a_d(t) \leqslant |x| \leqslant a(t), t) = \pm\tilde{V}, \quad V(a(t) < |x| < a_1, t) = 0. \tag{43}$$

Using the relation $V(x,t) = -\partial_x h(x,t)$, we can obtain the h-profile at any time $1/2 < t < 1$ by integrating equation (43) over x. The result describes a parabolic profile of h at $|x|<a_d(t)$, flanked by the linear profiles at $a_d(t)<|x|<a_1$ corresponding to the triangular structure of $h(x,t)$ of the first stage of the dynamics. At $t=1$ the parabolic profile takes over the whole interval $|x|<a_1$, and we obtain

$$h(x,t=1) = H - x^2, \quad |x| < a_1 = \sqrt{H}. \tag{44}$$

At $|x|>a_1$ the uniform solution holds:

$$h(|x|>a_1, t) = \Lambda t, \quad p(|x|>a_1, t) = \Lambda. \tag{45}$$

Now we evaluate the contributions of the uniform solution to the action, ΔS_u, and to the average height, $\Delta \bar{H}_u$, at $t=1$. As ℓ goes to infinity, we can neglect the difference

[6] We also obtained $\tau = 1/2$ analytically by solving the problem for a general τ and then minimizing the resulting action with respect to τ. These calculations are somewhat cumbersome, and we do not show them here.

J. Stat. Mech. (2023) 123202

between the total system length ℓ and the length of the domain of the uniform solution $\ell - 2a_1$, and obtain

$$\Delta S_u = \Lambda^2 \ell/2 \text{ and } \Delta \bar{H}_u = \Lambda. \tag{46}$$

The leading-order contribution of the soliton–antishock solution to the action is [4]

$$\Delta S_s = \frac{8\sqrt{2}}{3} \frac{H^{3/2}}{\sqrt{\tau}} = \frac{16H^{3/2}}{3}. \tag{47}$$

This contribution comes from the first stage of the process, $0 < t < 1/2$, while the second stage gives only a subleading contribution, which we neglect. However, the second stage, $1/2 < t < 1$, does contribute to $\bar{H}$. Using equation (44), we obtain

$$\Delta \bar{H}_s = \frac{4H^{3/2}}{3\ell}. \tag{48}$$

What remains to be done is to determine Λ, to collect the contributions to S and $\bar{H}$, and to eliminate H in favor of $\bar{H}$ and ℓ. In order to determine Λ, we use the local conservation of $p(x,t)$ evident in equation (13). Because of this local conservation law, the total soliton 'mass' (see equation (32)) must be equal to the integral of the solution (41) for $p(x,t)$ over x from -a_1 to a_1. This condition yields a remarkably simple result: $\Lambda = 4$, a constant value (up to small subleading corrections). Combining equations (46)–(48), we obtain

$$\bar{H} = 4 + \frac{4H^{3/2}}{3\ell}, \quad S = 8\ell + \frac{16H^{3/2}}{3}. \tag{49}$$

Eliminating H, we arrive at the leading-order result for the large-deviation function of $\bar{H}$ for branch 2 in the limit of large ℓ, which was announced in the second line of equation (31)

$$S = \left(4\bar{H} - 8\right) \ell. \tag{50}$$

This expression obeys the large-deviation scaling (10). As expected, the actions of branches 1 and 2 coincide at $\bar{H} = \bar{H}_c = 4$. Noticeably, their first derivatives with respect to $\bar{H}$ also coincide at this point. In addition, using equation (18), we see that equation (50) is consistent with $\Lambda = 4$, independently of $\bar{H}$, for branch 2. We will look into these peculiarities more carefully in section 5.4.

One applicability condition of equation (50) is the strong inequality $H \gg 1$. Using the first relation in equation (49), we can rewrite this strong inequality in terms of $\bar{H}$ and $\ell \gg 1$:

$$\bar{H} - 4 \gg 1/\ell. \tag{51}$$

J. Stat. Mech. (2023) 123202

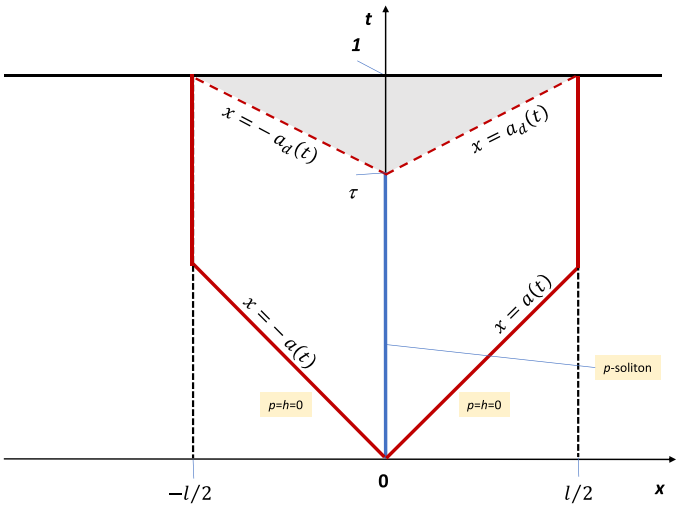

Figure 10. A space–time map of the optimal path of the system which determines the large-deviation function $S(\bar{H})$ of branch 3 in the large-ℓ limit. The notations are similar to those of figure 9.

This condition limits $\bar{H}$ from below. A condition on $\bar{H}$ from above distinguishes branch 2 from branch 3. It demands that the ordinary shocks of $V(x,t)$ do not collide with each other until $t=1$.[7] This condition can be written as $2\sqrt{\bar{H}}<\ell$ or, using equation (49),

$$\bar{H}-4<\frac{\ell^2}{6}\quad\text{at}\quad\ell\gg 1\,. \tag{52}$$

Now we proceed to a description of branch 3.

5.3. Branch 3

When the inequality (52) is violated, the two outgoing ordinary shocks of $V(x,t)$ collide with each other and merge at $x=\pm\ell/2$ (which is the same point of the ring) at some $t<1$. Upon the merger, a single stationary shock appears (see figure 10). Now the impact region of the soliton–antishock is the whole system, $2a_1=\ell$, and the external region of the uniform solution, characteristic of branch 2, does not appear here.

Most of the general formulae, derived in the context of branch 2, remain valid for branch 3. In particular, here too τ is determined by the condition that the weak discontinuities catch up with the ordinary shocks at $t=1$. The only difference is that $a_1=\ell/2$ now. Solving the equation $a_d(1)=a_1$, or

$$\sqrt{\frac{2H}{\tau}}\,(1-\tau)=\frac{\ell}{2}, \tag{53}$$

[7] While deriving equation (46) we demanded a *strong* inequality $2\sqrt{\bar{H}}\ll\ell$. However, when $\bar{H}\gg 1$, the main contribution to S and $\bar{H}$ comes from the soliton–antishock solution rather than from the uniform one. As a result, the strong inequality $2\sqrt{\bar{H}}\ll\ell$ becomes unnecessary, and a simple inequality suffices.

J. Stat. Mech. (2023) 123202

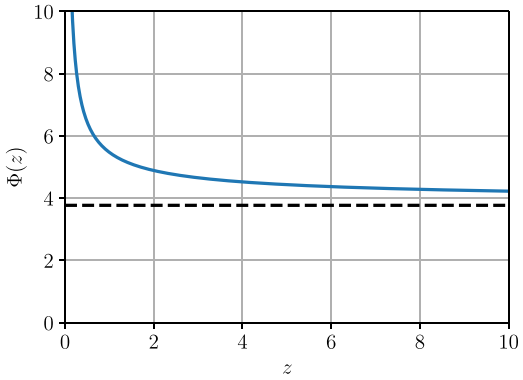

Figure 11. A plot of the function $\Phi(z)$ (blue) which enters equation (57) for the large-deviation function $S(\bar{H},\ell)$ for branch 3 in the large ℓ limit. The dashed line shows the large-z asymptote $\Phi(z\to\infty)=8\sqrt{2}/3$.

we obtain

$$\tau = 1 + \frac{\ell^2}{16H} - \frac{\ell\sqrt{\ell^2+32H}}{16H}, \tag{54}$$

so that τ depends on H and ℓ. Unsurprisingly, equation (54) yields $\tau = 1/2$ in the boundary case $H=\ell^2/4$, when the size $2a_1$ of the impact region of the soliton–antishock in an infinite system is equal to the system size ℓ. When H goes to infinity, τ approaches 1.

We will not repeat here all expressions for $h(x,t)$, $V(x,t)$ and $p(x,t)$ in different regions, and present only the expression for $h(x,1)$

$$h\,(x,1) = H - \frac{x^2}{2\,(1-\tau)}, \tag{55}$$

with τ from equation (54). Using this expression, we can evaluate $\bar{H}$. The action S remains the same as in the first equality in equation (47), and we obtain

$$\bar{H} = H - \frac{1}{24}\frac{\ell^2}{(1-\tau)}, \quad S = \frac{8\sqrt{2}}{3}\frac{H^{3/2}}{\sqrt{\tau}}. \tag{56}$$

Eliminating H from these relations and using equation (54), we arrive at a leading-order result for the large-deviation function $S(\bar{H},\ell)$ in the limit of large ℓ and very large $\bar{H}$, which was announced in the third line of equation (31)

$$S\,(\bar{H},\ell) = \bar{H}^{3/2}\Phi\left(\frac{\bar{H}}{\ell^2}\right), \quad \text{where} \quad \Phi\,(z) = \frac{2\sqrt{2}\,\left(9z+1+\sqrt{18z+1}\right)^{1/2}\left(36z+1+\sqrt{18z+1}\right)}{81z^{3/2}}. \tag{57}$$

In terms of $\bar{H}$, the condition $H>\ell^2/4$ becomes, in the leading order, $\bar{H}>\ell^2/6$. As a result, the function $\Phi(z)$ is defined for $z\geqslant 1/6$, and $\Phi(1/6)=4\sqrt{6}$. A graph of $\Phi(z)$ is depicted in figure 11.

J. Stat. Mech. (2023) 123202

In the limit of $\bar{H} \gg \ell^2 \gg 1$ equation (57) yields

$$S = \frac{8\sqrt{2}}{3}\bar{H}^{3/2} + \frac{4}{3}\bar{H}\ell + \dots. \tag{58}$$

The leading-order term of this expression coincides with the action for a single-point height H [4]. This is to be expected, because, for very large $\bar{H}$, τ approaches 1 and the difference between $\bar{H}$ and H becomes relatively small.

The expressions in equations (50) and (57) match in the leading order in ℓ at the boundary $\bar{H} \simeq \ell^2/6$ between the branches 2 and 3, both giving $(2/3)\ell^3 + O(\ell)$.

For completeness, we also present the optimal transition time τ in equation (54) in terms of $\bar{H}$ and ℓ

$$\tau\left(\bar{H},\ell\right) = 1 + \frac{\ell^2}{12\bar{H}} - \frac{\ell\sqrt{\ell^2 + 18\bar{H}}}{12\bar{H}}. \tag{59}$$

5.4. Dynamical phase transition

In this subsection we resolve the nature of the DPT between branches 1 and 2, which corresponds to the subcritical bifurcation from the uniform solution (19) to the leading-order soliton solution discussed in section 5.2. To this end we will have to focus on subleading corrections that we have previously ignored. We will also present the large-deviation scaling of $\mathcal{P}(\bar{H},L,T)$ in the limit of $T \to 0$ at fixed L, in the physical units.

As we have already noticed, the actions $S_1(\bar{H},\ell)$ and $S_2(\bar{H},\ell)$, described by the first and second lines of equation (31), coincide at $\bar{H} = \bar{H}_c = 4$ together with their first derivatives $\partial S_1(\bar{H},\ell)/\partial\bar{H}$ and $\partial S_2(\bar{H},\ell)/\partial\bar{H}$ at $\bar{H}_c = 4$. It would be incorrect, however, to conclude from here that the DPT between branches 1 and 2 at $\bar{H} = \bar{H}_c$ is of second order. Indeed, the supercritical first bifurcation of the uniform solution (19) to a solution with a single maximum of $h(x,1)$, the one with $q = 2\pi/\ell$ in equation (26), actually occurs, as $\ell \to \infty$, at much larger $\bar{H} \simeq \ell^2/16 \gg 4$. Furthermore, as follows from numerical minimization of equation (26), instability of *any* Fourier mode around the uniform solution can only occur at $\bar{H} \simeq 4.60334$ (for $q \simeq 1.34336$). It is not surprising, therefore, that at large but finite ℓ, and at a slightly shifted transition point $\bar{H}_c > 4$ where the actions of branches 1 and 2 are equal, the optimal paths $h(x,t)$ for branches 1 and 2, that we found numerically, are dramatically different, and their respective Lagrange multipliers Λ are not equal. The latter fact means, by virtue of equation (18), that at large ℓ we actually observe a first-order DPT not a second-order one.

To make sense of these facts, we recall that equation (50) for the action of branch 2 is merely a leading order asymptotic at $\ell \to \infty$. Subleading terms, so far unaccounted for, should remove the degeneracy of the leading-order results by breaking the accidental continuity of the first derivative $\partial S(\bar{H},\ell)/\partial\bar{H}$ at $\bar{H} = \bar{H}_c$, and rendering the corresponding bifurcation subcritical and the corresponding DPT first order. The subleading terms should also account for a slight shift of the critical point $\bar{H}_c$ to the right from its leading-order value $\bar{H}_c = 4$, as observed in our numerics.

J. Stat. Mech. (2023) 123202

Motivated by the large-H asymptotic of the upper tail of the exact short-time probability distribution of the one-point height $h(x=0,t=1)=H$ on the line, determined in [12], we can conjecture the following subleading terms of $S_2(\bar{H},\ell)$ at large ℓ:

$$S_2\left(\bar{H},\ell\right)=\left(4\bar{H}-8\right)\ell+BH^{1/2}+CH^{-1/2}+\ldots, \tag{60}$$

where $B>0$ and C are numerical constants $O(1)$, which are independent of ℓ. The condition $B>0$ is necessary for the equation

$$S_1\left(\bar{H}_{\rm c},\ell\right)=S_2\left(\bar{H}_{\rm c},\ell\right) \tag{61}$$

to have a solution for $\bar{H}_c$ close to 4 at large ℓ.

To verify equation (60), we plotted in figure 12 our large-ℓ numerical results for $\left[S_2(\bar{H},\ell)-\left(4\bar{H}-8\right)\ell\right]/\sqrt{H}$ versus H. A fair plateau at large H is observed, with $B\simeq 5.3>0$ found by fitting. Now, keeping the first subleading term in equation (60) and the leading-order dependence of H on $\bar{H}$ in equation (49), we can rewrite equation (60) in terms of $\bar{H}$ and ℓ:

$$S_2\left(\bar{H},\ell\right)=8\ell+4\left(\bar{H}-4\right)\ell+\left(\frac{3}{4}\right)^{1/3}B\left[\left(\bar{H}-4\right)\ell\right]^{1/3}+\ldots,\qquad \left(\bar{H}-4\right)\ell\gg 1. \tag{62}$$

Now equation (61) for the critical point becomes

$$\frac{1}{2}\left(\bar{H}_{\rm c}-4\right)^2\ell=\left(\frac{3}{4}\right)^{1/3}B\left[\left(\bar{H}_{\rm c}-4\right)\ell\right]^{1/3}+\ldots. \tag{63}$$

Its approximate solution,

$$\bar{H}_{\rm c}=4+6^{1/5}B^{3/5}\ell^{-2/5}+\ldots, \tag{64}$$

describes a small ℓ-dependent positive shift of the critical point from the leading-order value 4. This $\bar{H}_{\rm c}$ corresponds to

$$H=\left(\frac{9}{8}\right)^{2/5}B^{2/5}\ell^{2/5}+\ldots \tag{65}$$

of the branch 2 solution at the critical point. We observe that, for this solution, $H\to\infty$ as $\ell\to\infty$, guaranteeing applicability of our theory at large ℓ. Going back to the large-deviation scaling (10), we notice that there is now a small but finite jump $\sim\ell^{-2/5}$ of the derivative $\ell^{-1}\partial S/\partial\bar{H}$ of the effective rate function at the shifted critical point. The transition between branches 1 and 2, therefore, is of first order at large but finite ℓ. Such transitions with a finite but small jump of the first derivative of the free energy (or the action) are usually called weakly first order transitions [26].

By virtue of equation (18), the subleading correction in equation (62) also removes the degeneracy of the leading-order result $\Lambda=4$ by adding to it a small ℓ-dependent correction that goes to zero as $\ell\to\infty$.

Using equation (62), we plotted in figure 13 the actions of branches 1 and 2, normalized by $\ell\bar{H}^2$, in the vicinity of the $\bar{H}=\bar{H}_{\rm c}$. It is clearly seen that the subleading

J. Stat. Mech. (2023) 123202

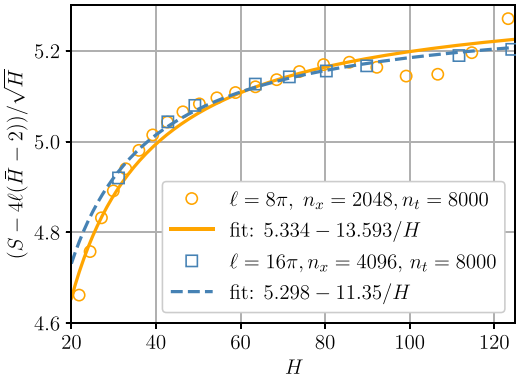

Figure 12. Numerical data from high-resolution optimal path computations at rescaled system sizes $\ell = 8\pi$ and 16π. Assuming an asymptotic expansion (60), the ordinate should be given by the subleading terms $B + C/H$ with constants B and C that are independent of ℓ and H. Accordingly, we performed least-squares fit with this functional form to the data for $20 \leqslant H \leqslant 125$. We observe a fair agreement for the two rescaled system sizes and determine $B \simeq 5.3$. For the smaller domain size $\ell = 8\pi$ there are small oscillations that may come from sub-subleading terms not included in equation (60).

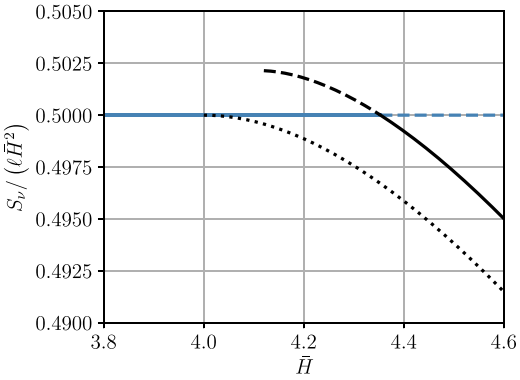

Figure 13. The rescaled actions $S_\nu/(\ell\bar{H}^2)$ for $\nu = 1$ and $\nu = 2$ versus $\bar{H}$ for a very long domain $\ell = 128\pi$. The result for $\nu = 1$ (branch 1) is shown by the blue lines, the prediction of equation (62) for $\nu = 2$ (branch 2) is shown by the black lines. The solid lines correspond to the global minima of the action, whereas the dashed lines correspond to local but not global minima of the action. The thin dotted line shows the asymptotic theoretical prediction for $S_2/(\ell\bar{H}^2) = (4\bar{H} - 8)\bar{H}^{-2}$ for $\ell \to \infty$.

correction removes the degeneracy and makes the DPT first-order. Furthermore, the predicted $\bar{H}_c$ from equation (64) for $\ell = 32\pi$, which is $\bar{H}_c \simeq 4.6$, is close to our numerical result $\bar{H}_c \simeq 4.57$ for this ℓ (see figure 7).

Note that our arguments in favor of the expansion (60) are far from rigorous. In particular, we cannot exclude a very slow (e.g. logarithmic) dependence of the coefficient B on H in equation (60) based only on the numerical evidence. However, our main conclusion about the first-order DPT between branches 2 and 3 seems robust.

J. Stat. Mech. (2023) 123202

To conclude this section, we present our large-deviation results, described by the first two lines of equation (31), in the physical units. Recall that, by taking the limit $T \to 0$ at fixed L, we have both $\varepsilon \propto T^{1/2} \to 0$ and $\ell \to \infty$. In this limit only the first two lines of equation (31) are relevant, and we obtain[8]

$$-\lim_{T\to 0} T \ln P\left(\bar{H}, L, T\right) = \frac{\nu^2}{D\lambda^2} L f\left(\frac{\lambda \bar{H}}{\nu}\right), \text{ where } f(w) = \begin{cases} w^2/2 & \text{for } w < 4, \\ 4w - 8 & \text{for } w > 4. \end{cases} \tag{66}$$

As we elaborated in this subsection, the DPT in equation (66) at $w = 4$ can be called an 'accidental' second-order DPT in the sense that the optimal paths that are responsible for the two branches in equation (66) transition into each other discontinuously, and that the differentiability of the rate function at the critical point emerges only in the limit $T \to 0$ at fixed L.

6. Small-ℓ asymptotics

We found that our numerical results on the second-order DPT at small ℓ, shown in figures 3 and 4 and described in section 4, can be understood in terms of a small-ℓ asymptotic solution of the OFM equations (12) and (13), which was previously found in the context of the one-point height distribution on a ring [10]. In this solution the interface is driven by a stationary dn^2 profile (see below) of p. The solution represents a finite-amplitude generalization of a weak sinusolidal modulation with $m = 1$ which results from the second-order DPT from the uniform solution. This solution is given by the following expressions[9]

$$h(x,t) \simeq Ht + 2\ln \mathrm{dn}\left[\frac{2K(k)\,x}{\ell}, k\right], \tag{67}$$

$$p(x,t) \simeq p_0(x) = \left[\frac{4K(k)}{\ell}\right]^2 \mathrm{dn}^2\left[\frac{2K(k)\,x}{\ell}, k\right], \tag{68}$$

where $K(k)$ is the complete elliptic integral of the first kind and $\mathrm{dn}(\ldots)$ is one of the Jacobi elliptic functions [27]. The elliptic modulus $k \in (0,1)$ is determined by H via the relation

$$\frac{8\left(2-k^2\right)K^2(k)}{\ell^2} = H. \tag{69}$$

The action of this solution as a function of k is [10]

$$S(k) = \frac{128}{3\ell^3} K^3(k)\left[2\left(2-k^2\right)E(k) - \left(1-k^2\right)K(k)\right]. \tag{70}$$

[8] Note the factor of T instead of the customary weak-noise factor $T^{1/2}$ on the left-hand side of equation (66).

[9] This solution is invalid inside narrow boundary layers in time at $t = 0$ and $t = 1$, but their contribution to the action is negligible.

J. Stat. Mech. (2023) 123202

At given $\ell \ll 1$, equations (69) and (70) determine S as a function of H in a parametric form. The critical point $\bar{H} = (2\pi/\ell)^2$ corresponds to $k = 0$, when equations (69) and (70) reduce to the uniform solution. $k > 0$ correspond to supercritical solutions.

In order to recast this dependence in terms of $S(\bar{H}, \ell)$, we need to express H through $\bar{H}$ and ℓ. Although equation (67) is formally inapplicable at $t = 1$, asymptotically as $\ell \to 0$ we still have

$$H - \bar{H} \simeq -\frac{1}{\ell} \int_{-\ell/2}^{\ell/2} 2 \ln \mathrm{dn} \left[\frac{2K(k)\, x}{\ell}, k \right] \mathrm{d}x = \frac{1}{2} \ln \frac{1}{1-k^2}. \tag{71}$$

where we have used a product formula for dn [28]. Using equations (69) and (71), we obtain

$$\bar{H}(k) = \frac{8\left(2-k^2\right) K^2(k)}{\ell^2} - \frac{1}{2} \ln \frac{1}{1-k^2}. \tag{72}$$

Equations (70) and (72) determine $S = S(\bar{H}, \ell)$ and were used in figure 3 to draw the theoretical curves for the action and Lagrange multiplier (via equation (18)) at $\ell = \pi/8$, which agree very well with the numerical action minimization results. Also shown is the asymptotic action

$$S\left(\bar{H}\right) \simeq \frac{8\sqrt{2}}{3} \bar{H}^{3/2} \tag{73}$$

as $\bar{H} \to \infty$, which agrees with equation (58) and can be obtained from equations (70) and (72) by considering the limit $k \to 1$ with $E(k) \to 1$ and $K(k) \simeq \frac{1}{2} \ln \frac{1}{1-k}$. As one can see from figure 4, the asymptotic relation (71) is not yet satisfied for the moderately small $\ell = \pi/8$: noticeably, the solution $h(x, 1)$ at the final time deviates from equation (67). However, the numerically found action is already accurately described by equations (70) and (72) because the difference between H and $\bar{H}$ is always subleading, at most $O(\sqrt{\bar{H}})$, at small ℓ.

7. Summary and discussion

We applied the OFM to evaluate analytically and numerically the short-time PDF $P(\bar{H}, L, t = T)$, and the optimal paths which dominate this PDF, of the KPZ interface on a ring. The short-time PDF has the scaling form (9), where $\varepsilon \sim T^{1/2}$ plays the role of the weak-noise parameter. The phase diagram of the system represents the $(\bar{H}, \ell = L/\sqrt{\nu T})$ plane. We were especially interested in the DPTs that occur in this system at sufficiently large positive $\lambda \bar{H} > 0$. We found that, depending on ℓ, these DPTs occur via either a supercritical or a subcritical bifurcation of the 'trivial' (uniform in space) optimal path of the KPZ interface. The supercritical bifurcations dominate at very small ℓ, while the subcritical bifurcations dominate at very large ℓ. In these two limits we obtained asymptotic analytical solutions for the optimal paths of the system, evaluated the resulting action and verified the analytical results numerically. We also found that, as T goes to zero at constant L, the PDF acquire a simple large-deviation

J. Stat. Mech. (2023) 123202

form (11) and (66). Interestingly, the rate function $f(\bar{H})$ exhibits, at a critical value of $\bar{H} = \bar{H}_c(\ell)$, a DPT which is *accidentally* second order.

In the (much more complicated) region of intermediate $\ell = O(1)$ we observed numerically both supercritical and subcritical bifurcations of the uniform solution. This region of the phase diagram is currently out of reach of analytical theory. It would be very interesting, but challenging, to determine the complete phase diagram of the system in this region. In particular, it would be interesting to locate, somewhere between $\ell = 16\pi$ and $\ell = 32\pi$, at least one critical point $(\bar{H}_*, \ell_*)$ where the second-order DPT curve $\bar{H}_c^{(2)}(\ell)$ ends when it meets the first-order DPT curve $\bar{H}_c^{(1)}(\ell)$.

These tasks will become more feasible if this problem, as described by equations (12)–(16), joins the list of similar large-deviation OFM problems for the KPZ equation that have been solved exactly by the inverse scattering method (ISM) [18, 20]. Indeed, as was previously found in [7], a canonical Hopf–Cole transformation brings equations (12) and (13) into the nonlinear Schrödinger equation in imaginary space and time. Therefore, equations (12) and (13) belong to a family of completely integrable models. The only problem (but potentially a big one) is to adapt the ISM to a finite system with periodic boundaries and to accommodate the problem-specific boundary conditions (14) and (16). The exact solution would provide full analytic control of the subleading corrections to the action of branch 2, which are currently half-empiric.

It would be very interesting to explore the possibility of extending to the spatially averaged KPZ interface height some of the recent 'stochastic integrability' approaches, which led, for selected initial conditions, to exact representations for the complete statistics of the *one-point* interface height [29–37].

Finally, we can try to put our results into a broader perspective of DPTs in large deviations of macroscopic systems far from equilibrium. The second-order DPT in the present periodic KPZ system occurs when the unstructured optimal height profile $h(x,t) = \bar{H}t$ uniformly translating in the vertical direction gives way to spatially non-uniform height profiles via a supecritical bifurcation. This transition can be compared with second-order DPTs in large deviations of the current [38–41] and of the system activity [42] in some diffusive lattice gas models with periodic boundaries. In each of these systems a spatially uniform state gives way to a non-uniform state via a supercritical bifurcation. The structured states, however, have the form of simple travelling waves, whereas in the present system they are more complicated.

A second-order DPT is also observed in large deviations of the *one-point* height of a KPZ interface in an infinite system with Brownian initial conditions [7, 8, 11, 20]. The underlying bifurcation is also supercritical, but the transition mechanism is quite different. Indeed, the optimal height profiles $h(x,t)$ are non-uniform and essentially non-stationary both below and above the transition, while the transition is accompanied by a mirror symmetry breaking.

Similarly, the first-order DPT that we reported here differs from its counterpart in large deviations of the one-point height of a KPZ interface *at a shifted point* in the KPZ equation with Brownian initial conditions [11]. These differences between mechanisms of different DPTs of the same order call for a better understanding of DPTs in general.

J. Stat. Mech. (2023) 123202

Acknowledgments

The authors thank Eldad Bettelheim and Naftali R Smith for useful discussions. This research was supported by the program 'Advanced Research Using High Intensity Laser-Produced Photons and Particles' (ADONIS) (CZ.02.1.01/0.0/0.0/16019/0000789) of the European Regional Development Fund (ERDF) (PS) and by the Israel Science Foundation (Grant No. 1499/20) (BM).

Appendix. Numerical methods

Our numerical procedure for finding solutions h and p of the OFM problems (12)–(16) can be summarized as follows. To compute numerical solutions to the boundary-value problem for h and p for given ℓ and $\bar{H}$, we use a refined version of the popular Chernykh–Stepanov back-and-forth iteration algorithm [43] as described in detail in [44], using the language of partial differential equation-constrained optimization. The idea is to interpret the back-and-forth iterations—fixing Λ and solving equation (12) forward in time with fixed p, and equation (13) backward in time with fixed h until convergence—as adjoint [45] gradient evaluations $\delta S/\delta p$ of the action functional with fixed Λ,

$$S[p] = \frac{1}{2}\int_0^1 \mathrm{d}t \int_0^\ell \mathrm{d}x\, p^2(x,t) - \Lambda \int_0^\ell h[p](x,1)\,\mathrm{d}x, \tag{A1}$$

with the height profile $h = h[p]$ determined for a given p through equation (12). This interpretation allows us to use automatic update step-size control (here, Armijo line search [46]) and preconditioning for faster convergence (here, the L-BFGS method [47]). Conceptually, one fixes Λ in this formulation and obtains the corresponding average height value $\bar{H}$ *a posteriori*.

For large ℓ we find multiple solutions for the same $\bar{H}$, and the action $S(\bar{H},\ell)$ of the optimal solution as a function of $\bar{H}$ becomes nonconvex for some $\bar{H}$. Nonconvexity of the rate function $S(\bar{H})$ is an issue because minimizing the functional (A1) effectively computes the Legendre–Fenchel transform of the rate function at Λ, which may diverge in this case. Therefore, we add a penalty term to the action, leading to the so-called augmented Lagrangian formulation [48]

$$S[p] = \frac{1}{2}\int_0^1 \mathrm{d}t \int_0^\ell \mathrm{d}x\, p^2(x,t) - \Lambda\left(\int_0^\ell h[p](x,1)\,\mathrm{d}x - \ell\bar{H}\right) + \frac{\mu}{2}\left(\int_0^\ell h[p](x,1)\,\mathrm{d}x - \ell\bar{H}\right)^2, \tag{A2}$$

and solve multiple minimization problems for increasing penalty parameters μ. In this formulation, one can directly prescribe $\bar{H}$ at the cost of solving multiple optimization problems, and it is usable regardless of convexity of the rate function, or in other words regardless of bijectivity of the map between $\bar{H}$ and Λ.

The formulation (A1) is more convenient for tracing solution branches: one initializes the optimization on an already found solution on a given branch and slightly

J. Stat. Mech. (2023) 123202

changes Λ. In order to trace branches close to the transition region for large ℓ in the nonconvex case, we temporarily reparameterize the observable as described in [49] with reparameterizations $g(z) = \ln\ln z$ or $g(z) = 1 - \exp\{-(z - 3.5)\}$.

Within this general framework, we use a pseudo-spectral code with spatial resolution n_x to solve equations (12) and (13), with an exact integration of the diffusion terms through an integrating factor in Fourier space. An explicit second-order Runge–Kutta integrator with n_t equidistant steps is used in time. The gradient of the action functional is evaluated exactly on a discrete level ('discretize, then optimize'). A Python source code which illustrates the optimization methods in a simple toy problem can be found in a public GitHub repository [50] and it is explained in [51].

An important property of equations (12) and (13) is their exact integrability [7, 18, 20]. It is convenient to exploit it for monitoring the accuracy of our numerical discretization scheme. To this end we followed in time the first five conserved quantities of the continuous system [18]

$$c_1 = \int p \, \mathrm{d}x \tag{A3}$$

$$c_2 = \int p \partial_x h \, \mathrm{d}x \tag{A4}$$

$$c_3 = \int p \left[\partial_{xx} h + \frac{1}{2} (\partial_x h)^2 + \frac{1}{2} p \right] \mathrm{d}x \tag{A5}$$

$$c_4 = \int p \left[\partial_{xxx} h + \frac{3}{2} \partial_x h \partial_{xx} h + \frac{1}{4} (\partial_x h)^3 + \frac{1}{2} \partial_x p + \frac{3}{4} p \partial_x h \right] \mathrm{d}x \tag{A6}$$

$$\begin{aligned} c_5 = \int p \Big[& \partial_{xxxx} h + \frac{3}{2} (\partial_{xx} h)^2 + \frac{1}{8} (\partial_x h)^4 + 2 \partial_x h \partial_{xxx} h + \frac{3}{2} (\partial_x h)^2 \partial_{xx} h \\ & + \frac{1}{8} \partial_x h \left[2 \partial_x p + 3 p \partial_x h \right] + \frac{1}{4} \left[2 \partial_{xx} p + 3 \partial_x p \partial_x h + 3 p \partial_{xx} h \right] \\ & + \frac{1}{8} p (\partial_x h)^2 + \frac{1}{2} p \left[\partial_{xx} h + \frac{1}{2} (\partial_x h)^2 + \frac{1}{2} p \right] \Big] \mathrm{d}x \end{aligned} \tag{A7}$$

for the optimal paths that we calculated numerically. The code conserves c_1 up to machine precision, but the higher c_i are only approximately conserved. For instance, for the optimal path shown in the top row of figure 6, for the nonzero quantities c_3 and c_5, we obtain conservation within 0.3% and 0.6%, respectively, for our numerical solution. For other optimal paths at different $\bar{H}$ and ℓ, we observe a similar, sufficiently high, accuracy of the conservation of c_3 and c_5 in our numerical results. (The quantities c_2 and c_4 should theoretically be equal to 0 for all times due to the initial condition $h(x, t = 0) = 0$ and periodic boundary conditions in space. They are less convenient, therefore, for the analysis of relative accuracy of numerical results.)

Due to the fixed and small time interval $0 \leqslant t \leqslant 1$, intrinsic to the problem of short-time statistics of the KPZ interface, there are no adverse consequences of the violation of exact conservation of the quantities c_i. This violation would be a more serious problem if we were to attempt to advance the solution until long times, $t \gg 1$. For this reason we have not derived an integrable discretization in space and time, but such discretizations do exist. They are described in detail, for example in the monograph [52].

J. Stat. Mech. (2023) 123202

References

[1] Kolokolov I V and Korshunov S E 2007 *Phys. Rev.* B **75** 140201(R)
[2] Kolokolov I V and Korshunov S E 2008 *Phys. Rev.* B **78** 024206
[3] Kolokolov I V and Korshunov S E 2009 *Phys. Rev.* E **80** 031107
[4] Meerson B, Katzav E and Vilenkin A 2016 *Phys. Rev. Lett.* **116** 070601
[5] Kamenev A, Meerson B and Sasorov P V 2016 *Phys. Rev.* E **94** 032108
[6] Le Doussal P, Majumdar S N, Rosso A and Schehr G 2016 *Phys. Rev. Lett.* **117** 070403
[7] Janas M, Kamenev A and Meerson B 2016 *Phys. Rev.* E **94** 032133
[8] Krajenbrink A and Le Doussal P 2017 *Phys. Rev.* E **96** 020102(R)
[9] Meerson B and Schmidt J 2017 *J. Stat. Mech.* 103207
[10] Smith N R, Meerson B and Sasorov P 2018 *J. Stat. Mech.* 023202
[11] Smith N R, Kamenev A and Meerson B 2018 *Phys. Rev.* E **97** 042130
[12] Smith N R and Meerson B 2018 *Phys. Rev.* E **97** 052110
[13] Hartmann A K, Le Doussal P, Majumdar S N, Rosso A and Schehr G 2018 *Europhys. Lett.* **121** 67004
[14] Meerson B and Vilenkin A 2018 *Phys. Rev.* E **98** 032145
[15] Asida T, Livne E and Meerson B 2019 *Phys. Rev.* E **99** 042132
[16] Smith N R, Meerson B and Vilenkin A 2019 *J. Stat. Mech.* 053207
[17] Hartmann A K, Meerson B and Sasorov P 2019 *Phys. Rev. Res.* **1** 032043(R)
[18] Krajenbrink A and Le Doussal P 2021 *Phys. Rev. Lett.* **127** 064101
[19] Hartmann A K, Meerson B and Sasorov P 2021 *Phys. Rev.* E **104** 054125
[20] Krajenbrink A and Le Doussal P 2022 *Phys. Rev.* E **105** 054142
[21] Lamarre P Y G, Lin Y and Tsai L-C 2023 *Probab. Theor. Rel. Fields* **185** 885
[22] Schorlepp T, Grafke T and Grauer R 2023 *J. Stat. Phys.* **190** 50
[23] Kardar M, Parisi G and Zhang Y-C 1986 *Phys. Rev. Lett.* **56** 889
[24] Cunden F D, Facchi P and Vivo P 2016 *J. Phys. A: Math. Theor.* **49** 135202
[25] Whitham G B 2011 *Linear and Nonlinear Waves* (Wiley)
[26] Binder K 1981 *J. Stat. Phys.* **24** 69
[27] Wolfram Research Inc. 1999 Jacobi Elliptic Functions (available at: https://mathworld.wolfram.com/JacobiEllipticFunctions.html)
[28] Wolfram Research Inc. 1998 Elliptic Functions JacobiDN (available at: https://functions.wolfram.com/EllipticFunctions/JacobiDN/08/)
[29] Sasamoto T and Spohn H 2010 *Phys. Rev. Lett.* **104** 230602
[30] Calabrese P, Le Doussal P and Rosso A 2010 *Europhys. Lett.* **90** 20002
[31] Dotsenko V 2010 *Europhys. Lett.* **90** 20003
[32] Amir G, Corwin I and Quastel J 2011 *Commun. Pure Appl. Math.* **64** 466
[33] Calabrese P and Le Doussal P 2011 *Phys. Rev. Lett.* **106** 250603
[34] Le Doussal P and Calabrese P 2012 *J. Stat. Mech.* P06001
[35] Imamura T and Sasamoto T 2012 *Phys. Rev. Lett.* **108** 190603
[36] Imamura T and Sasamoto T 2013 *J. Stat. Phys.* **150** 908
[37] Borodin A, Corwin I, Ferrari P and Vető B 2015 *Math. Phys. Anal. Geom.* **18** 20
[38] Bertini L, De Sole A, Gabrielli D, Jona-Lasinio G and Landim C 2005 *Phys. Rev. Lett.* **94** 030601
[39] Bodineau T and Derrida B 2005 *Phys. Rev.* E **72** 066110
[40] Hurtado P I and Garrido P L 2011 *Phys. Rev. Lett.* **107** 180601
[41] Zarfaty L and Meerson B 2016 *J. Stat. Mech.* 033304
[42] Lecomte V, Garrahan J P and van Wijland F 2012 *J. Phys. A: Math. Theor.* **45** 175001
[43] Chernykh A I and Stepanov M G 2001 *Phys. Rev.* E **64** 026306
[44] Schorlepp T, Grafke T, May S and Grauer R 2022 *Phil. Trans. R. Soc.* A **380** 20210051
[45] Plessix R-E 2006 *Geophys. J. Int.* **167** 495
[46] Armijo L 1966 *Pac. J. Math.* **16** 1
[47] Liu D C and Nocedal J 1989 *Math. Program.* **45** 503
[48] Hestenes M R 1969 *J. Optim. Theory. Appl.* **4** 303
[49] Alqahtani M and Grafke T 2021 *J. Phys. A: Math. Theor.* **54** 175001
[50] Schorlepp T, Tong S, Grafke T and Stadler G 2023 GitHub repository (available at: https://github.com/TimoSchorlepp/sharp-extreme-event)
[51] Schorlepp T, Tong S, Grafke T and Stadler G 2023 *Stat. Comput.* **33** 137
[52] Suris Y B 2003 *The Problem of Integrable Discretization: Hamiltonian Approach* (Springer)

J. Stat. Mech. (2023) 123202